Quasimolecular x-ray spectroscopy for slow Cl^{16+}-Ar collisions

R. Schuch*
Physikalisches Institut, Universität Heidelberg, D-6900 Heidelberg, Federal Republic of Germany

M. Meron, B. M. Johnson, and K. W. Jones
Brookhaven National Laboratory, Upton, New York 11973

R. Hoffmann†
Physikalisches Institut, Universität Heidelberg, D-6900 Heidelberg, Federal Republic of Germany

H. Schmidt-Böcking
Institut für Kernphysik, Universität Frankfurt, D-6000 Frankfurt, Federal Republic of Germany

I. Tserruya
Physics Department, Weizmann Institute of Science, Rehovot, Israel
(Received 17 August 1987)

Quasimolecular x-ray transitions into the $1s\sigma$ orbital of the Cl^{16+}-Ar collision system were measured in coincidence with scattered particles for collision energies of 20, 10, 5, and 2.5 MeV. The acceleration-deceleration method was used to produce K-shell vacancy bearing projectiles at low velocities. Because K-shell vacancies were brought into the collisions, the excited states of the transient quasimolecules could decay by x-ray emission either on the incoming or on the outgoing parts of the collision trajectory. The resulting interference structures in the quasimolecular x-ray spectra are clearly observed for impact parameters between 600 and 3000 fm. The analysis of these spectra has produced the first experimental determinations of $2p\pi$-$1s\sigma$ transition energies as a function of internuclear distance. Details of the experimental procedure, results, and analysis are presented; the velocity and impact-parameter dependencies of spectral decay widths are investigated; and the effects of collision broadening for quasimolecular x rays are discussed.

I. INTRODUCTION

Long ago it was realized that the electronic states formed in slow collisions between heavy ions and atoms could be described as being similar to those of very-short-lived quasimolecules. This quasimolecular view of atomic collisions emerged from the study of many inner-shell processes, such as excitation by radial and rotational coupling, and emission of positrons, electrons, and x rays during the formation of such quasimolecules.[1–4] A generally accepted condition to form quasimolecular states is that the ion velocity should be small compared to the Bohr electron orbital velocity in the respective shell.

Previous experimental studies of quasimolecular effects have yielded interesting information about the energy states of the quasimolecules, but only within the framework of particular theoretical models.[5,6] A long-standing but elusive goal of this research has been a direct spectroscopy of the molecular orbitals (MO's); that is, the experimental determination of the transition energies as a function of internuclear distance during the formation and deformation of a quasimolecule.[7] A detailed account of the first direct determinations of quasimolecular transition energies is the subject of this paper.

In 1972, when the discovery of MO x-ray bands was first reported,[8,9] it was widely believed that it should be easy to observe sharp structure in x-ray–emission spectra which could be directly related to MO transition energies. Several approaches were tried. There was the search for an end point in the MO x-ray spectrum at the united-atom (UA) transition energy.[10,11] The lack of an end point[12] was explained[13] by collision broadening of the x-ray transition similar to the broadening of atomic lines described by Weiskopf.[14] Then there were speculations[15] about a peak at the UA transition energy resulting from transitions induced by the rotating coordinate frame. The existence, however, of such a peak in the MO x-ray spectrum could be verified neither experimentally[16] nor theoretically.[17] One promissing possibility was opened by studies of the anisotropy of the angular distribution of MO x rays with respect to the beam axis.[18] Encouragingly, these results showed a clear enhancement in the region of UA transition energies, but disappointingly the theoretical explanations[19] of this structure are so complex that spectroscopic information from such data is not presently obtainable.

The first successful approach to quasimolecular x-ray spectroscopy[20,21] was made possible by recent accelerator developments which allow for two previously incompatible experimental conditions: (1) a projectile which bears a K-shell vacancy so that the production and decay of inner-shell vacancies are decoupled, and (2) an incident projectile velocity which is slow compared to the Bohr orbital velocity of inner-shell electrons so that collision

broadening is considerably reduced, and the quasimolecular picture is applicable. Highly charged ion beams are usually created by accelerating negative or low-charge-state ions to high energy, and then using gas or foil stripping to remove most (or all) of the remaining electrons. Large accelerators can easily produce K-vacancy-bearing projectiles (even for very heavy ions), but only through stripping at very high velocities. By decelerating after stripping (the "accel-decel" technique[22]), the two required conditions are met. For the experiments discussed here, acceleration-deceleration beams provided both hydrogenlike projectiles (Cl^{16+}) and low collision velocities ($v_p/v_K = 0.31$, 0.22, 0.16, and 0.11 at energies of 20, 10, 5, and 2.5 MeV, respectively, where v_p is the projectile velocity and v_K is the target K-electron Bohr velocity).

Bringing the K-shell vacancy into the collision has two very favorable consequences. First, the emission probability is considerably enhanced, since the probability of having a vacancy in the $1s\sigma$ orbital can be close to unity. Second, $1s\sigma$ vacancies can be filled either on the incoming or on the outgoing parts of the collision trajectory. That is, MO x rays with the same energy E_x can be emitted at two different collision times, either at a particular time on the way in or at a time corresponding to the same internuclear distance R (and the same transition energy ΔE) on the way out. The coherent sum of the corresponding transition amplitudes produces an interference structure in the x-ray spectrum which was observed to be strongly dependent on both the impact parameter and the velocity of the collision. Direct determinations of MO x-ray transition energies E_x were obtained earlier from the analysis of observed interference structures by applying the stationary-phase approximation[21] (SPA) and the uniform asymptotic approximation (UAA).[23] The combination of these two analytical approaches has yielded experimentally determined $1s\sigma$-$2p\pi$ MO transition energies for the Cl-Ar collision system over a wide range of internuclear distances R, independent of any modeling of the MO x-ray emission.

The major thrust of this paper is a full presentation of the experimental data and a detailed account of the spectroscopic analysis. In addition, the special aspect of collision broadening of MO x-ray emission beyond the classical limit is discussed. For the first time, the spectral decay width Γ is obtained from these experiments for each impact parameter b and collision velocity v. The experimentally determined dependencies of Γ on both b and v are compared with theoretical predictions.

II. EXPERIMENTS

Beams of Cl^{16+} ions at energies from 20 to 2.5 MeV were produced by the dual MP tandem facility at Brookhaven National Laboratory using the four-stage acceleration-deceleration mode of operation[22] (see Fig. 1). The first tandem (MP6) was operated in a conventional two-stage mode with a positive terminal voltage to allow for the first stage of acceleration to the terminal, where foil stripping removes several electrons, and the second stage of acceleration, which produces beams of energetic positive ions. The second tandem (MP7) was operated with a negative terminal voltage to provide the third stage of acceleration to the MP7 terminal, where foil stripping removes more electrons, and finally deceleration (the fourth stage), which produces the desired beams of low-energy, highly charged ions. For the production of Cl^{16+} ions at energies of 20, 10, 5, and 2.5 MeV, the voltage settings of the two tandems, as well as the intermediate-charge states and energies, are given in Table I.

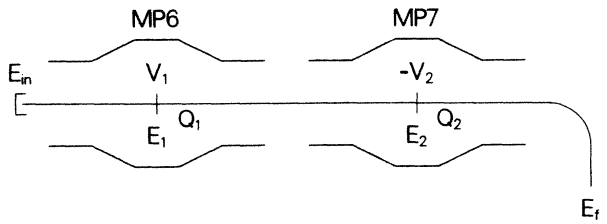

$$E_1 = E_{in} + V_1$$

$$E_2 = E_{in} + V_1 + Q_1(V_1 + V_2)$$

$$E_f = E_{in} + V_1 + Q_1(V_1 + V_2) - Q_2V_2$$

FIG. 1. Schematic diagram of the BNL tandems when used in the four-stage acceleration-deceleration mode of operation to produce low-velocity, highly charged ion beams.

In principle, the four-stage acceleration-deceleration method could be used to produce essentially zero-energy beams, but, in practice, a lower-energy limit is imposed by transmission losses due to emittance growth. For example, Table II traces the estimated beam emittance from the ion source, through the three stages of acceleration and stripping, and after the deceleration and extraction. The normalized emittance and beam energy are also given at each point to distinguish between velocity-dependent and velocity-independent effects. Note that there are two large emittance growths of nearly an order of magnitude from 3.2 to 22 mm mrad, and from 6 to 48 mm mrad. The first occurs with negligible change in beam energy at the point of MP6-terminal stripping, when the 10-MeV beam undergoes multiple scattering in the 5-$\mu g/cm^2$ carbon foil. The second occurs because of a defocusing effect during deceleration, when the beam energy decreases from 160 to 2.5 MeV. Note also that since the beam energy is much higher (160 MeV) at the

TABLE I. MP7 terminal voltages (V_{MP7}), maximum terminal energies (E_{max}), and analyzed beam currents (I_f) for the low-velocity Cl^{16+} ions produced by the dual MP tandem facility (MP6 and MP7) at Brookhaven National Laboratory (BNL), operating in the four-stage acceleration-deceleration mode. In all cases, negative Cl ions were injected into MP6 at energies of 120 keV, V_{MP6} was 9.5 MV, and the charge-state component selected from the beam produced by MP6 was Cl^{8+}.

	Energy (MeV)			
	20	10	5	2.5
V_{MP7} (MV)	−8.2	−9.5	−10.1	−10.4
E_{max} (MeV)	151	162	166	169
I_f (nA)	3.4	2.8	2.0	1.5

TABLE II. Estimated beam emittance, normalized emittance, and beam energy at various stages of injection, acceleration, stripping, deceleration, and extraction for a 2.5-MeV Cl^{16+}-ion beam produced in the BNL four-stage acceleration-deceleration mode of operation.

	Beam emittance (mm mrad)	Normalized emittance (mm mrad $MeV^{1/2}$)	Beam energy (MeV)
Ion source (exit)	25	10	0.15
MP6 terminal (before strip)	3.2	10	10
MP6 terminal (after strip)	22	70	10
MP7 terminal (before strip)	5.5	70	160
MP7 terminal (after strip)	6	76	160
Exit of MP7 (after deceleration)	48	76	2.5
Exit of MP7 (after aperture)	23	36	2.5

terminal of MP7, there is negligible beam emittance growth during foil stripping. At the exit of MP7 a 30-mm aperture reduces beam emittance at the expense of beam current, but the final emittance of 23 mm mrad is nearly identical to the 25 mm mrad at injection. Deceleration to lower beam energies would cause both greater emittance growth during deceleration, and larger reductions in beam current at the exit aperture.

A schematic view of the experimental setup for measuring the impact-parameter-dependent MO x-ray–emission probability is shown in Fig. 2. After magnetic analysis to select the Cl^{16+} ions, the beam was collimated with slits C1 and C2. After passing C2 an electrostatic deflector was used to bend the Cl^{16+} beam component by 12° so that it would pass through collimator C3, which was set to horizontal and vertical openings of 10×10 mm^2. Other charge-state fractions produced by background-gas interactions upstream of the electrostatic deflector, as well as by slit scattering, were thereby eliminated. Next, the beam passed through three circular collimators with fixed diameters of 6, 6, and 4 mm, and entered the interaction region, which was a 20-mm-long gas cell with a needle inlet for the Ar target atoms. Emerging from the gas cell, the beam then traveled through three more circular collimators with increasing diameters of 8.5, 10, and 13 mm. This allowed for transmission of projectile ions at scattering angles up to a maximum of 7.5°. Unscattered particles and those which interacted only at very large impact parameters then passed through a circular aperture with a diameter of 3 mm and finally stopped in a Faraday cup. The relative longitudinal positions of the collimators are indicated in Fig. 2.

The raw data for the determination of the impact-parameter dependence of MO x-ray production were obtained by recording x-ray events in coincidence with scattered particles. X rays produced in the target cell were

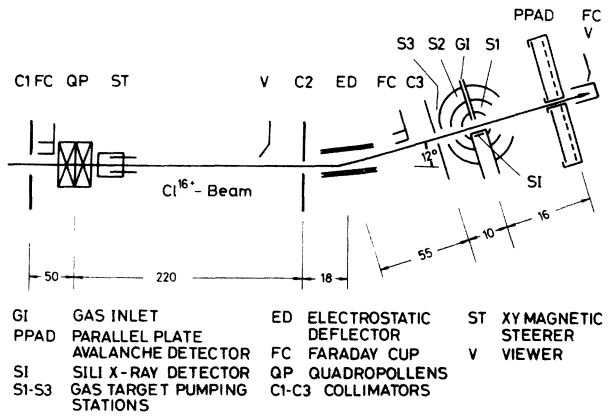

FIG. 2. Schematic diagram of the experimental setup. Indicated distances are in cm.

detected at 90° to the beam direction by a 200-mm^2 Si(Li) detector with 280-eV resolution at 5.9 keV. The geometrical solid angle of the detector was determined to be $\Omega/4\pi=0.045$. A 0.038-mm-thick aluminum absorber was used to suppress both characteristic x rays and photons produced by radiative electron capture (REC). This was necessary to reduce dead time and pileup in the detector because characteristic x-ray and REC production are much more probable than MO x-ray production.

The scattered particles were recorded with a parallel-plate avalanche detector (PPAD).[24] The anode of the PPAD, which was divided into 16 concentric rings, was designed so that ring width increased with diameter such that the scattering-angle resolution was a constant $\Delta\theta/\theta=0.1$ for each ring. In principle, it was possible to simultaneously record scattered particles corresponding to 16 different small ranges of b, but, in practice, the signals from two rings (or even three rings for small b, i.e., large θ) were added together to improve statistics.

As shown in Table III, the transverse opening of the beam-defining aperture C1 was not the same for all beam energies. C1 had to be enlarged as the beam energy was decreased, because deceleration has a defocusing effect, which reduces transmission. Between runs at the two higher (20 and 10 MeV) and the two lower (5 and 2.5 MeV) energies, the collimator C1 openings in both the horizontal and vertical dimensions were enlarged from 5 to 30 mm. This resulted in a maximum beam-divergence increase in each direction from 1.3 to 5.9 mrad (that is, from 0.074° to 0.34°), and a slit-acceptance increase from 3.7 to 22 mm mrad. Note that at the lowest energy of 2.5 MeV, the slit acceptance of 22 mm mrad is comparable to the estimated beam emittance from Table II of 36 mm mrad at the exit of MP7.

If the same C1 openings used at 20 and 10 MeV had been kept when the beam energy was decreased to 2.5 MeV, then 90% of the beam would have been lost due to the emittance growth. Fortunately, the scattering angle corresponding to a given impact parameter also increases with decreasing beam energy. This means that larger beam divergencies can be tolerated at lower beam energies. When compared to the 10% scattering-angle reso-

TABLE III. Collimator C1 and C2 aperture openings in horizontal and vertical dimensions, corresponding one-dimensional beam divergences, and resulting acceptances for each beam energy. As indicated in Fig. 2, the distance between C1 and C2 was 270 cm.

	Energy (MeV)			
	20	10	5	2.5
C1 opening (mm)	5×5	5×5	30×30	30×30
C2 opening (mm)	2×2	2×2	2×2	2×2
Divergence (mrad)	1.3	1.3	5.9	5.9
Divergence (deg)	0.074	0.074	0.34	0.34
Acceptance (mm mrad)	3.7	3.7	22	22

lution for each ring of the PPAD, a beam divergence of 0.34° is of negligible influence. Since the signals from two or three rings were added together, however, there was concern that the interference structure might have been "washed out" if the ranges of θ (and corresponding ranges of b) were too great. This was not the case. As shown in the following, the expected interference structures are clearly observed.

Scattering angles were converted into impact parameters by first using a pure Coulomb potential (b_C) and then a Bohr screened potential (b_{sc}) for neutral Cl and Ar atoms.[25] The differences between b_C and b_{sc} were as much as 20% at the largest b. Since the projectiles are nearly bare nuclei, an average value of b_C and b_{sc} was used to determine b.

Figure 3 shows a typical N_{REC}/N_p pressure dependence, where N_p is the total number of scattered particles. The optimal target pressure was determined from the pressure dependence of the REC yield, N_{REC}.[26] This was appropriate because for H-like projectiles the REC yield should have the same target pressure dependence as MO x rays. The correction factor for the fraction of the beam which lost its K vacancy before entering the interaction region [i.e., the field of view of the Si(Li) detector] was also obtained from the measured pressure dependencies of REC yields. The Ar pressure in the gas cell, as measured with a capacitance manometer, was adjusted to be in the range of 1–10 mTorr.

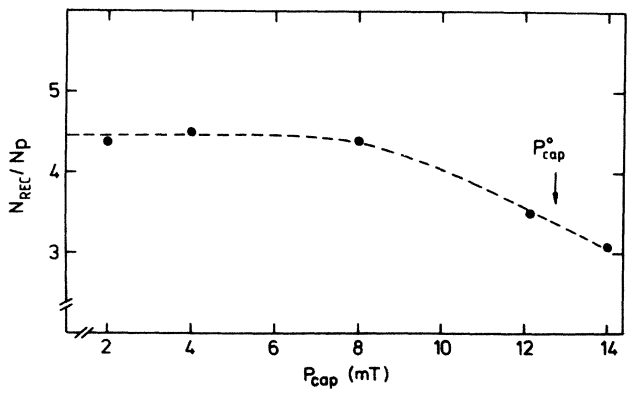

FIG. 3. The yield of REC x rays (normalized by scattered particles) vs target pressure.

Because Cl^{15+} and lower-charge-state ions would not bring a K-shell vacancy into the interaction region, it was very important to maintain low gas pressures between the electrostatic deflector and the gas cell. For this reason the cylindrical target cell was surrounded by two separately pumped cylinders to provide three stages of differential pumping (indicated as S3, S2, and S1 in Fig. 2). The upstream lengths of S3, S2, and S1 were 200, 10, and 15 mm, and the pressures were of order 10^{-6}, 10^{-5}, and 10^{-4} Torr, respectively. The pressure upstream of C3 (fourth stage of differential pumping) was typically of order 10^{-7} and always less than 10^{-6} Torr.

III. RESULTS

Figure 4 shows a singles (noncoincidence) x-ray spectrum produced by collisions between 2.5-MeV Cl^{16+} projectiles and Ar target atoms. The displayed spectrum has not been corrected for the effects of the aluminum absorber, which reduced the x-ray yields by factors of 10^4 and 10^3 at the Cl $K\alpha$ and REC peak energies, respectively. The REC peak is obviously the most prominent line in the spectrum. The shoulder at double the REC energy is caused by REC pulse pileup.

The expected positions[27] of the two-electron, one-photon transitions ($K\alpha\alpha$) are indicated by arrows. As their name implies, these transitions require initial states with at least two electrons in the L shell and none in the K shell. The $K\alpha\alpha$ lines are not observed in these experiments because the transition probabilities are small ($\simeq 10^{-5}$), and the capture-plus-excitation probabilities of

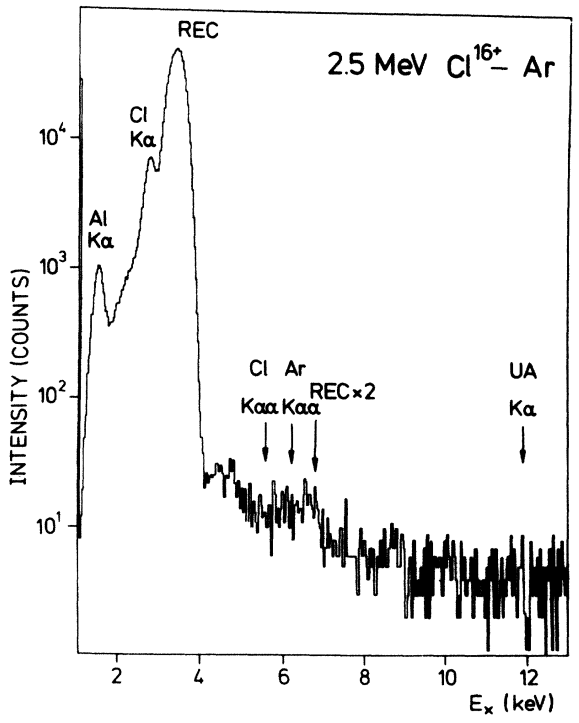

FIG. 4. A singles x-ray spectrum from collisions of 2.5-MeV Cl^{16+} with Ar. The united-atom (UA) $K\alpha$ transition energy is indicated.

producing the initial state are also very low. The lines would have been observable if metastable $2s^1$ states, which might be copiously produced in the beam-foil interaction at the terminal of MP7, had survived the deceleration and transport to the gas cell. This was not the case, because there were long flight times afforded by the low projectile velocities of the acceleration-deceleration beams.

Figure 4 also shows that the expected MO x-ray structure (in the energy range from 4 to 10 keV) is barely discernible from the background continuum in the singles spectra. Fortunately, however, this is not true for the coincidence spectra. Figure 5 shows two-dimensional contour plots of coincidence time (abcissa) versus x-ray energy (ordinate) for rings 3–9 of the PPAD. For this range of impact parameters (800–3000 fm) the REC and Cl $K\alpha$ features (2–4 keV) show no time structure, but the MO x-ray events exhibit very distinct time peaks. Events caused by REC pulse pileup and other sources of random background are therefore easily separated from events attributable to molecular-orbital x-ray production. The number of true coincident MO x-ray events for each energy above 4 keV was corrected for (1) attenuation in the Al absorber, (2) solid angle and efficiency of the Si(Li) detector, and (3) fractional loss of K vacancies due to background-gas interactions between the electrostatic deflector and the gas cell.

The MO x-ray–emission probabilities dP/dE_x for each measured range of b were then determined from

$$dP/dE_x = 4\pi N(E_x)\varepsilon(E_x)/N_p\Delta\Omega_x ,$$

where $N(E_x)$ is the number of true coincidence events at a given energy E_x, $\varepsilon(E_x)$ is the x-ray–absorption factor, N_p is the yield of scattered particles (corrected for slit scattering), and $\Delta\Omega_x$ is the solid-angle efficiency of the x-ray detector. These probabilities are plotted in Figs. 6, 7, and 8 for collisions at 20, 5, and 2.5 MeV. The corresponding plots for the 10-MeV collisions were shown earlier.[20] The error bars in Figs. 6–8 represent only the statistical uncertainty, but there could be systematic errors. For example, the absolute values could be low by as much as a factor of 2 because the PPAD might accept particles scattered outside the field of view of the x-ray detector. In addition, the uncertainties in the determination of Si(Li)-detector solid angle and projectile K-vacancy loss were ±30% and ±20%, respectively. A possible anisotropy of the MO x-ray emission is neglected as well. It was measured in a separate experiment[28] and found to be less than 30%.

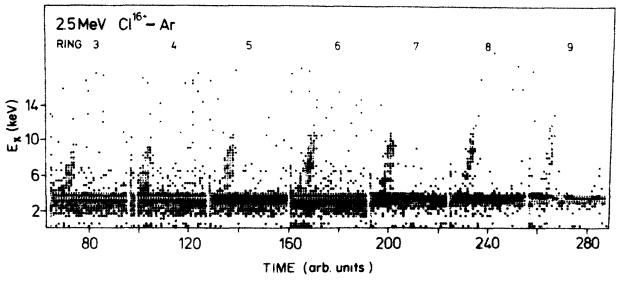

FIG. 5. Two-dimensional event plots of coincidence time vs x-ray energy for different rings of the PPAD particle detector.

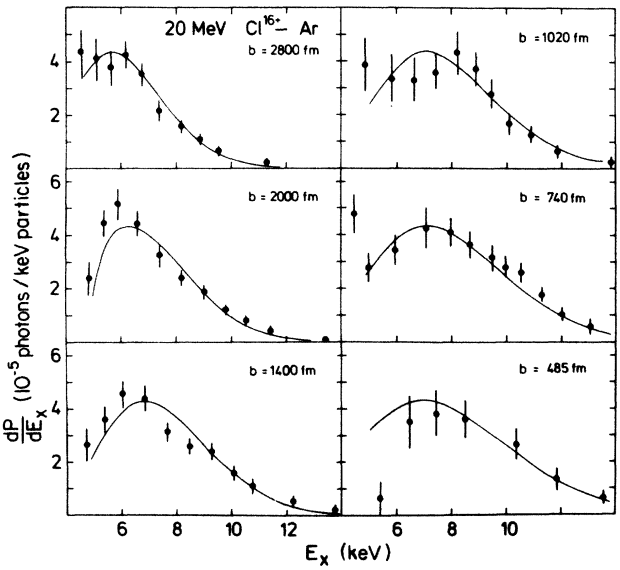

FIG. 6. X-ray–emission probabilities as a function of x-ray energy at different impact parameters for the beam energy of 20 MeV.

The spectra show oscillations which are increasing in frequency both with decreasing impact parameter and decreasing velocity. This behavior is typical for a quantum-mechanical interference of amplitudes at different parts of the collision. A photon from a transition into the $1s\sigma$ state can be emitted on incoming and

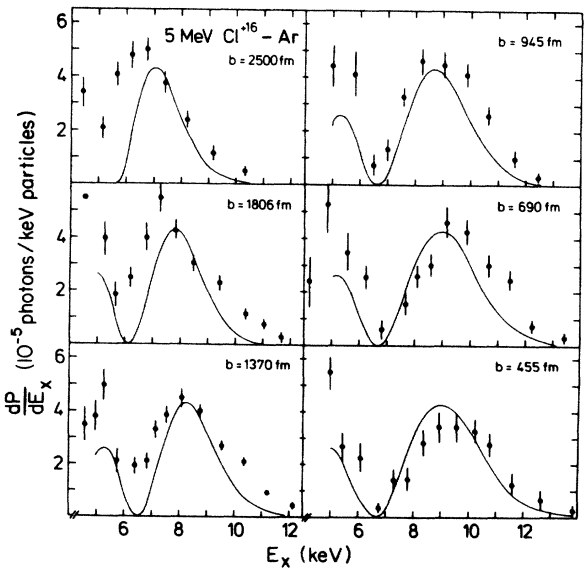

FIG. 7. X-ray–emission probabilities as a function of x-ray energy at different impact parameters for the beam energy of 5 MeV.

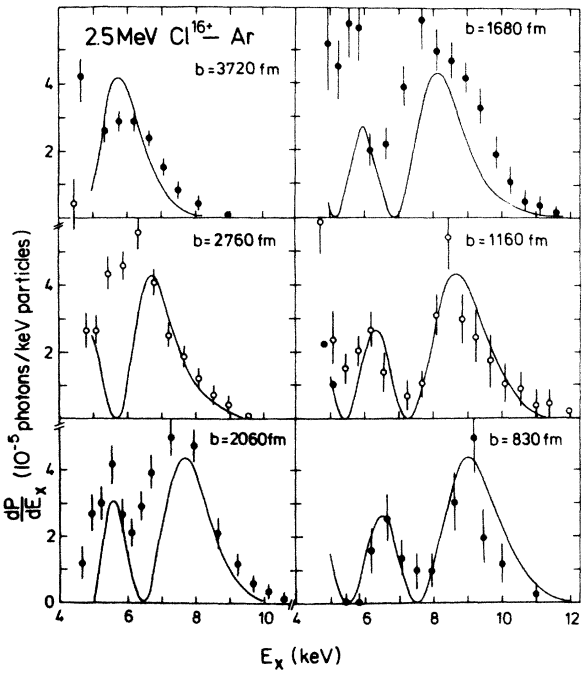

FIG. 8. X-ray–emission probabilities as a function of x-ray energy at different impact parameters for the beam energy of 2.5 MeV.

outgoing parts of the trajectory with the same frequency. In a classical double-slit experiment, when photons are allowed to pass through either slit, an interference pattern is produced. Here a similar interference effect (see Figs. 6–8) is modulated by the phase difference between the two parts of the transition amplitude, which is determined by the collision times and transition energies. A quantitative description of the photon spectra is given below.

IV. DISCUSSION

In traditional spectroscopy the determination of transition energies is a separate issue from the extraction of transition probabilities. The same is true in MO x-ray spectroscopy. At low collision velocity, the typical MO x-ray spectrum (e.g., Fig. 8) exhibits an oscillatory pattern that changes over into a "nearly exponential" decay near the classical cutoff frequency ω_c. The spectra exhibit a high-energy tail beyond $E_c=\hbar\omega_c$ due to the coupling of the photon emission to the collision dynamics. The oscillatory pattern and the changeover region can be analyzed to determine transition energies, while transition probabilities can be extracted from the absolute values of the MO x-ray–emission probabilities.

A. Transition energies

Following the theoretical description of Weisskopf[14] for the collision-induced broadening of optical lines, Macek and Briggs[12] obtained the frequency-dependent photon-emission amplitude $D_{if}(\omega)$ for a transition between states i and f as a Fourier transform of the dipole transition amplitude $D_{if}(R(t))$. This can be written[14] as

$$D_{if}(\omega)=\frac{1}{2\sqrt{2\pi}}\int_{-\infty}^{+\infty}dt\, D_{if}(R(t)) \times\exp\left[-\Gamma\frac{t}{2}+i\int_0^t[\omega-\omega_{if}(\tau)]d\tau\right], \tag{1}$$

where $E_x=\hbar\omega$ is the photon energy. The frequency

$$\omega_{if}(\tau)=[E_i(R(\tau))-E_f(R(\tau))]/\hbar ,$$

where E_i and E_f are energy eigenvalues of states i and f, which are functions of the internuclear separation R. The dipole transition amplitude is given by

$$D_{if}(R(t))=\langle\psi_i(r,R)\,|\,\mathbf{D}\,|\,\psi_f(r,R)\rangle , \tag{2}$$

where $\mathbf{D}$ the dipole operator acting between the initial and final electronic wave functions $\psi_i(r,R)$ and $\psi_f(r,R)$.

The energy dependence of the photon intensity for transitions into state f at a given impact parameter b is given by[14]

$$I(E_x)\propto E_x\,|\,D_{if}(E_x)\,|^2 . \tag{3}$$

Both the dipole transition amplitude $D_{if}(\omega)$ and the transition frequency ω_{if} are unknown. Therefore the Fourier transform given in Eq. (1) cannot be obtained directly without assuming a specific model. The intent here, however, is to obtain model-independent results for the MO transition energies. Previously, two approximations, the SPA and the UAA, have been used to obtain the MO transition energy $E_x=E_i(R(t))-E_f(R(t))$ for specific values of R.

1. Stationary phase approximation

The first experimental determination of $2p\pi$-$1s\sigma$ transition energies as a function of R (internuclear distance) (Ref. 21) were made using the SPA. This theoretical approach was originally applied to MO x-ray transitions by Macek and Briggs,[12] and developed further by Fritsch and Wille.[29]

The SPA is traditionally used to approximate integrals of the form given in Eq. (1), whenever the time variation is dominated by the exponential term. The fact that the spectra shown in Figs. 6–8 show oscillations, which are increasing in frequency with decreasing velocity, clearly demonstrates that molecular orbitals are well defined during the collision process. According to the Heisenberg uncertainty principle, this means that the product of collision time and transition frequency ω_{if} must be much greater than unity. Therefore the exponential term in Eq. (1) is rapidly oscillating and the condition for application of the SPA is fulfilled.

It is shown in Appendix A that the application of the SPA to Eq. (1) results in

$$D(\omega,b) \propto \cos\left[\phi+\frac{\pi}{4}\right], \tag{4}$$

where

$$\phi=\int_0^{t_b} t\frac{d\omega_{if}(t)}{dt}dt \ . \tag{5}$$

The stationary phase point t_b is given by $\omega_{if}(t_b)=\omega=E_x/\hbar$. The index b indicates the implicit dependence of t_b on the trajectory, which, in turn, depends on the impact parameter b. Substitution of Eq. (4) into Eq. (3) yields

$$I(\omega,b) \propto \omega\cos^2\left[\phi+\frac{\pi}{4}\right], \tag{6}$$

which is the relation used to analyze the data.

Relation (6) indicates an oscillatory pattern in the experimental spectrum, where (to a first approximation) the separation between an adjacent maximum and minimum is given by

$$\Delta\phi=|\phi_{\max}-\phi_{\min}|=\frac{\pi}{2}=\left|\int_{t_{\min}}^{t_{\max}} t\frac{d\omega_{if}(t)}{dt}dt\right| . \tag{7}$$

Assuming that ω_{if} is a reasonably well-behaved function of t, and that $|\omega_{\max}-\omega_{\min}|$ is reasonably small, then the integral in Eq. (7) can be approximated by

$$\Delta\phi=\frac{\pi}{2}\simeq t_{\text{mid}}\,|\omega_{\max}-\omega_{\min}| \ , \tag{8}$$

where t_{mid} is defined by

$$\omega_{if}(t_{\text{mid}})=\tfrac{1}{2}(\omega_{\max}+\omega_{\min}) \ . \tag{9}$$

The values of $\omega_{\max}$ and $\omega_{\min}$ are obtained by visual inspection of the spectra. Equation (8) is used to determine values of t_{mid} for each spectrum. Since the impact parameter and collision velocity are well defined, the internuclear distances $R(t_{\text{mid}})$ are determined. Finally, Eq. (9) is used to find the value of $\omega_{if}(t_{\text{mid}})$, which is the value of ω_{if} corresponding to $R(t_{\text{mid}})$.

The open symbols in Fig. 9 are the results of this analysis, where $\Delta E(R)=\hbar\omega_{if}(t(R))$. Note that more than one ΔE can be extracted from some spectra, and that values of $R(t_{\text{mid}})$ in no way correspond to the distance of closest approach $R(0)$. Furthermore, as shown in Appendix A, the SPA breaks down near $R(0)$. Therefore this analytical approach is incapable of yielding values of ω_{if} close to the united-atom limit.

2. *Uniform asymptotic approximation*

The uniform asymptotic approximation was used to extend the range of R [down to $R(0)$] over which $2p\pi$-$1s\sigma$ transition energies could be determined.[23] The UAA is a more general treatment, which subsumes the SPA. It was initially introduced by Chester, Friedman, and Ursell,[30] developed by Connor and Marcus,[31] and applied to MO transitions by Fritsch and Wille[29] and by Devdariani, Ostroskii, and Niehaus.[32] Fritsch and Wille[29] and Niehaus[33] first pointed out the analogy between the interference effects in MO x-ray spectra and in the rainbow (or rainbow scattering).

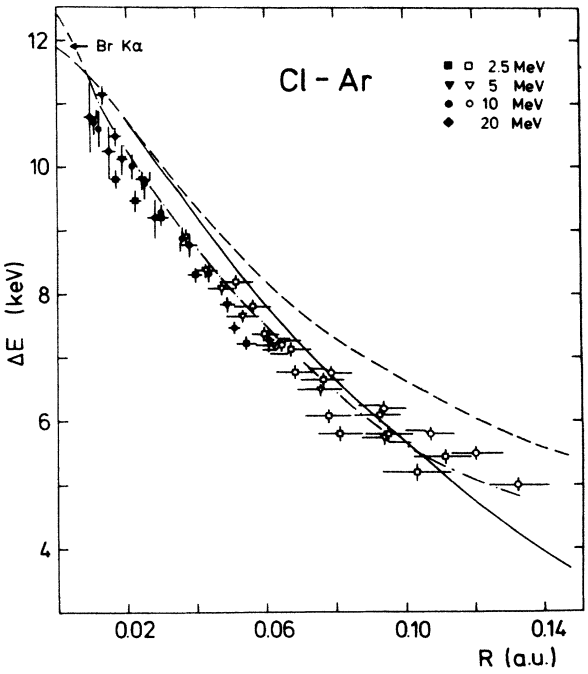

FIG. 9. Transition energies between $1s\sigma$ and $2p\pi$ MO states as a function of internuclear distance R. The dashed-dotted line is from DFS calculations for the $2p\pi$-$1s\sigma$ transition; solid and dashed lines are scaled from $H^+ + H$ for the $2p\sigma$-$1s\sigma$ and $2p\pi$-$1s\sigma$ transition, respectively.

A short description of the UAA approach to the present problem is presented in Appendix B. Application of the UAA to Eq. (1) now results in

$$D(\omega,b) \propto \mathrm{Ai}(-x) \ , \tag{10}$$

where Ai is an Airy function, and

$$x=(-\tfrac{3}{2}\phi)^{2/3} \ , \tag{11}$$

and where ϕ is the same function defined earlier in Eq. (5). For $\omega=\omega_{if}(0)$, at the distance of closest approach $R(0)$, x is equal to zero.

Note that Eq. (10) is the UAA equivalent of Eq. (4), which was obtained using the SPA, but it is shown in Appendix B that Eq. (4) is an asymptotic limit of Eq. (10). Therefore the more general UAA approach could be applied not only near $R(0)$, but also over the oscillatory part of the spectrum (i.e., for larger R), reiterating the results of the previous SPA analysis.

Substituting Eq. (10) into Eq. (3) yields

$$\frac{I(\omega,b)}{\omega} \propto \mathrm{Ai}^2(-x) \ , \tag{12}$$

which is the relation used for the UAA analysis of the data. As mentioned previously, visual inspection of the data in Figs. 6–8 shows that $I(\omega)$ changes over from an oscillatory function at small $\omega=E_x/\hbar$ to a nearly exponential tail at larger ω. This is Airy-function behavior,

where the changeover occurs near $\omega=\omega_{if}(0)$, which corresponds to $x=0$. The value ω_1 for which $I(\omega)/\omega$ has a maximum just before the changeover corresponds to x_1, which is the first maximum of $\mathrm{Ai}(-x)$. Comparing Eq. (12) for these two values of ω yields

$$\frac{I(\omega_{if}(0))}{\omega_{if}(0)}\frac{\omega_1}{I(\omega_1)}\approx\left[\frac{\mathrm{Ai}(0)}{\mathrm{Ai}(-x_1)}\right]^2=0.44\ . \tag{13}$$

If the data are replotted after dividing by E_x, then a plot equivalent to $I(\omega)/\omega$ results. Using (13) it is possible to determine $\omega_{if}(0)$ simply by inspecting these plots of $I(\omega)/\omega$ in the region above ω_1, and finding the location at which $I(\omega)/\omega$ drops to 0.44 of its value at the relevant maximum, as is shown (for example) in Fig. 10.

The solid symbols in Fig. 9 are the results of this analysis, where $\Delta E\equiv\Delta E(R(0))=\hbar\omega_{if}(0)$. Only one ΔE is extracted from each spectrum, and the corresponding R is the distance of closest approach, $R(0)$. Note that the UAA analysis yields results for smaller values of R than the SPA. Fortunately, R values between 2500 and 3000 fm are covered by both approaches. Note the good agreement between the extracted values of MO x-ray transition energies in the region of overlapping R. This agreement between results obtained using the UAA and SPA, and derived from different portions of different spectra, indicates the reliability of both schemes, each in its own useful range. Rather than choosing one method over the other, both methods should be used in combination, so as to extract the maximal amount of information from the experimental data.

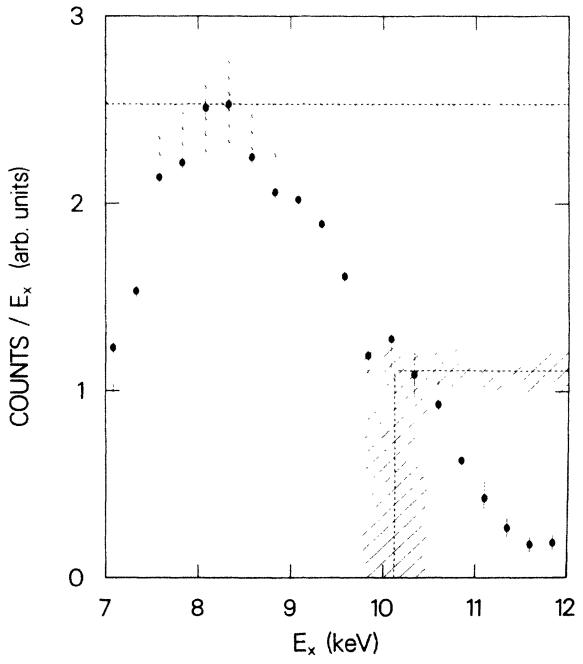

FIG. 10. Expanded portion of a typical MO x-ray spectrum ($E_p=5$ MeV, $b=255$ fm) divided by the MO x-ray energy E_x. Application of the UAA Airy analysis method is indicated (see text and Appendix B). The upper dashed horizontal line represents the peak height. The lower horizontal line is located at 0.44 peak height and its intercept with the measured spectrum yields $E_x(0)=\hbar\omega(0)$, the MO transition energy at the internuclear distance of closest approach. The shaded areas represent experimental uncertainties.

The measured $\Delta E(R)$ are compared with calculated quasimolecular transition energies in Fig. 9. The two upper curves were obtained by a scaling from H^+-H energy curves.[34] The binding energies and the R values are scaled following the procedure of Heinig *et al.*[35] The dashed and solid lines represent results for the $1s\sigma$-$2p\sigma$ and $1s\sigma$-$2p\pi$ transition energies, respectively. The dashed-dotted curve is for the $1s\sigma$-$2p\pi$ transition from a Dirac-Fock-Slater (DFS) calculation[36] for a 15-times-ionized Cl-Ar quasimolecule. Note that there is good agreement with the experimental data, especially for the $1s\sigma$-$2p\pi$ transition. The $1s\sigma$-$2p\pi$ transition is expected to be dominant, because the $2p\pi$ orbital has twice as many electrons as $2p\sigma$, and the $1s\sigma$-$2p\sigma$ transition matrix element approaches zero as R increases. At small R, $2p\sigma$ and $2p\pi$ are nearly degenerate, so that the transition energies, and therefore the solid and dashed curves in Fig. 9, are nearly the same.

B. Spectral shape

As an alternative to the procedures described above, it might seem that fitting an Airy function to the shape of the spectra in Figs. 6–8 would result in a more reliable determination of $\Delta E(R)$. That is, why not fit Eq. (12) to the spectra? Because, as shown in Eqs. (11) and (5), the parameter x in the Airy function of Eq. (12) is itself a function of $\omega_{if}(t)$, i.e., a function of $\Delta E(R)$. Therefore such a fit could be performed only after $\Delta E(R)$ is known.

Since $\Delta E(R)$ has been experimentally determined (see Fig. 9), $I(\omega)$ can be calculated using the Airy-function formalism, and compared to the spectra in Figs. 6–8 to test whether the spectral shapes are well represented. The procedure would be to first determine $R(t)$ from the collision trajectory. This is possible because the mean impact parameter b and the collision velocity v are known for each spectrum. Using this $R(t)$ in conjunction with values of $\Delta E(R)$ from Fig. 9 yields $\omega_{if}(R(t))$, which is equal to $\omega_{if}(t)$. Now Eqs. (5) and (11) could be used to generate values of x as a function of ω. Substitution of these x into Eq. (12) yields $I(\omega)$, which should reproduce the experimental spectrum. The procedure is straightforward, but would be very tedious, since the entire process would have to be repeated for each spectrum.

While the procedure outlined above can give a qualitative indication of how well each spectrum is reproduced by an Airy function, it would not show how the results scale with b and v. A far greater insight into the general behavior of $I(\omega)$ versus b and v would be gained if the parameter x in Eq. (12) could be approximated by a closed analytical expression. This can be done using the following simplified approach, proposed by Devdariani *et al.*[32]

Figure 9 indicates that $\Delta E(R)$ can be approximated by a linear function of R over a wide range of internuclear distances, i.e.,

$$\Delta E(R)\simeq\hbar\omega_{\mathrm{UA}}-FR\ . \tag{14}$$

A fit of Eq. (14) from $R=0$ to 0.075 a.u. (0–4000 fm) to

the results shown in Fig. 9 yields $\hbar\omega_{UA}=11.5$ keV and $F\simeq 66$ keV per atomic unit of length (or $F\simeq 2430$ a.u.). Because the Coulomb interaction-strength parameter $Z_1Z_2e^2/Eb$ is very small for all the collisions studied here, it is justifiable to assume a straight-line trajectory,

$$R(t)=\left[b^2+\frac{2E}{m}t^2\right]^{1/2}\approx b+\frac{E}{mb}t^2\approx R(0)+\frac{E}{mb}t^2 . \tag{15}$$

After dividing by $\hbar$, substitution into Eq. (14) yields

$$\omega_{if}(t)=\omega_{UA}-\frac{F}{\hbar}R(0)-\frac{FE}{\hbar mb}t^2=\omega(0)-\alpha t^2 , \tag{16}$$

where $\omega(0)=\omega_{UA}-FR(0)/\hbar$ is the frequency at $t=0$ for the given trajectory. Now, substituting Eq. (16) into Eq. (5) and then using Eq. (11) for a final substitution in Eq. (12) yields

$$I(\omega)\propto\omega\,\mathrm{Ai}^2\left[\frac{\omega-\omega(0)}{\alpha^{1/3}}\right] . \tag{17}$$

The solid lines in Figs. 6–8 were plotted using relation (17), where the normalization constant was provided by comparison with one spectrum ($E_p=2.5$ MeV, $b=830$ fm), and then kept constant for all beam energies and impact parameters. The general shape and the scaling with both collision velocity and impact parameter are well reproduced by the solid lines in Figs. 6–8.

C. Collision broadening

Due to the coupling of the photon emission to the collision dynamics, all of the MO x-ray spectra in Figs. 6–8 display a nearly-exponential tail that extends beyond the classical cutoff energy E_c. This is a typical example of the so-called collision broadening[12–14,29,37–40] which inhibited the early attempts to measure MO x-ray transition energies.[10,11]

For a total MO x-ray–emission spectrum E_c is equal to E_{UA}. For a differential MO spectrum measured at a specific impact parameter b, however, E_c is equal to $\Delta E(R(0))$, the MO transition energy at the distance of closest approach. A common and convenient decay-width definition is $\Gamma_{1/2}$, the difference between E_c and the energy at which the spectral amplitude has fallen off by $\frac{1}{2}$.[12,29] The $\Gamma_{1/2}$ obtained from the present data are plotted versus impact parameter in Figs. 11(a)–11(d). In general, $\Gamma_{1/2}$ could be a function of both b and v. The present results, however, exhibit little or no dependence on b. The solid lines in Fig. 11 show the results of weighted average fits to the data and are consistent with the assumption of no impact-parameter dependence.

A variety of theoretical methods based on Weisskopf's theory of collision broadening[14] have been used to examine the behavior of the MO x-ray–emission amplitude in the classically forbidden region.[12,29,37] These models predict different functional forms for the shape of the high-energy tails in MO x-ray spectra. One test of these models would be to fit the predicted functional forms to the data, but the extracted Γ would be model dependent. An alternative and preferable approach is to compare predicted and experimental values of $\Gamma_{1/2}$. Müller[37] has predicted that (in a.u.)

$$\Gamma_{1/2}(b,v)=2(\ln 2)v(R_{MO}^2+b^2)^{-1/2} , \tag{18}$$

where $R_{MO}=0.071$ a.u. (3760 fm). The dashed lines in Fig. 11 show the predictions of Eq. (18) plotted versus b. The exhibited impact-parameter dependence of the experimental decay widths is well represented by both the solid and the dashed curves. The present results cannot distinguish between no b dependence and the weak b dependence predicted by Eq. (18).

Figure 12 shows the velocity dependence of $\Gamma_{1/2}(0,v)$. The points represent the weighted average fits to the experimental results (see solid lines in Fig. 11). All of the theoretical models predict a velocity dependence of the form

$$\Gamma_{1/2}(v)\propto v^{\alpha} , \tag{19}$$

where α ranges from 1 to 0.5.[12,29,37,38] The dashed curve in Fig. 12 is the prediction of Eq. (18) (i.e., $\alpha=1$).

Macek and Briggs[12] discussed total MO x-ray production for ions traveling through solids. Their results predict $\alpha=0.5$ and a functional form

$$\Gamma_{1/2}(v)\simeq\tfrac{1}{3}(v\,d\,\Delta E/dR)^{1/2} , \tag{20}$$

where $d\,\Delta E/dR$ is evaluated close to E_c. The dotted curve in Fig. 12 is the prediction of Eq. (20) using

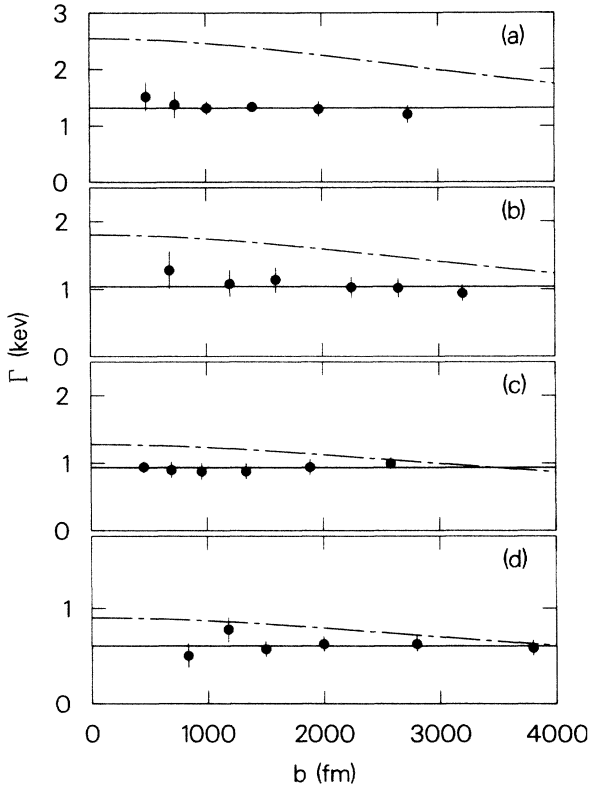

FIG. 11. Spectral decay width $\Gamma_{1/2}$ vs impact parameter b for beam energies of (a) 20, (b) 10, (c) 5, and (d) 2.5 MeV. The solid lines are weighted averages of the experimental results. The dashed lines are predictions of the Müller formula (Ref. 37).

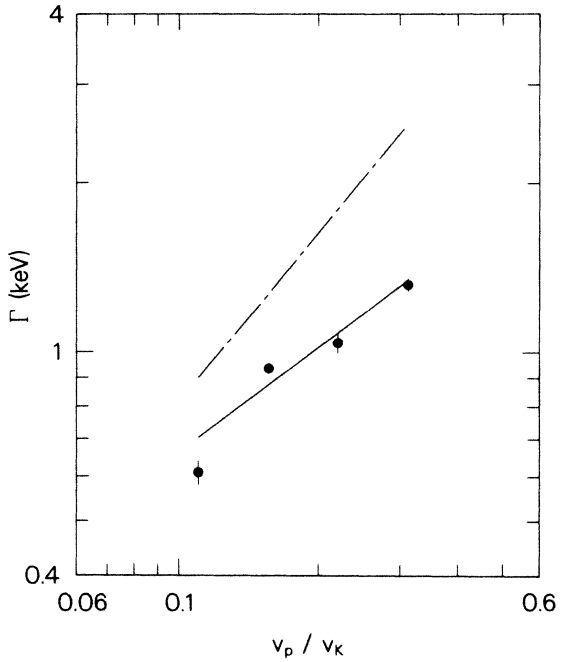

FIG. 12. Spectral density width $\Gamma_{1/2}$ as a function of the normalized collision velocity v_p/v_K. The points are weighted averages of constant-b results (see Fig. 11). The solid line is a least-squares fit to the points. The dashed (upper) and dotted (lower) lines represent the results from the models of Müller (Ref. 37) and Macek (Ref. 12), respectively.

$d\Delta E/dR=2430$ (in a.u.), as in Eq. (14).

The solid curve in Fig. 12 was obtained by fitting relation (19) to the experimental points, yielding a value of $\alpha=0.6\pm0.1$. This is in good agreement with the value of $\alpha=0.67$ obtained by Fritsch and Wille[29] using an Airy-function analysis (as used in the uniform asymptotic approximation). The fitted value is also close to $\alpha=0.58$ obtained from an empirical analysis of total MO x-ray cross-section data by Vincent and Greenberg.[40]

D. Transition probabilities

In these experiments, since the absolute number of true coincidence events was recorded as a function of energy, MO x-ray transition rates and probabilities can also be extracted from the data. In the earlier work[21,23] only transition energies were studied.

One approach to estimating MO x-ray–emission probabilities is to use the quasistatic approximation (QA). This treatment starts with the oversimplified assumption that x rays of energy E_x are only emitted when transitions occur at a certain internuclear distance $R(E_x)$, where $E_x=\hbar\omega_{if}(R(E_x))$. Assuming that a $1s\sigma$ vacancy exists, the QA emission probability is

$$\frac{dI(b,E_x)}{dE}=2\frac{\Gamma_x(E_x)}{v_R(b,E_x)}\frac{dR}{\hbar d\omega_{if}}(b,E_x)\ , \tag{21}$$

where Γ_x is the radiative transition rate between states i and f and v_R is the radial collision velocity. The factor of 2 arises from the incoming and outgoing parts of the trajectory where the photon transition can occur. Note that interference effects, which form the foundation of the SPA and UAA approaches, are completely ignored in the QA.

The QA is only useful for estimating the total emission probability integrated from an $E_{x\,min}$ to infinity. Integrating Eq. (21) yields

$$I(b,E_{x\,min})\simeq 2\Gamma_x(E_{x\,min})\Delta R(b,E_{x\,min})/v\ , \tag{22}$$

where v is the projectile velocity, $\Gamma_x(E_{x\,min})$ is the averaged radiative transition rate, and $\Delta R(b,E_{x\,min})\simeq[R^2(E_{x\,min})-b^2]^{1/2}$. $R(E_{x\,min})$ is the internuclear distance for the emission of an x-ray with energy equal to $E_{x\,min}$. Because the $1s\sigma$ vacancy may be transferred to the $2s\sigma$ orbital during the collision, the integrated MO x-ray emission probability is given by

$$P_{MO}(b,E_{x\,min})=P_{1s\sigma}I(b,E_{x\,min})\ , \tag{23}$$

where $P_{1s\sigma}$ is the probability that the vacancy remains in the $1s\sigma$ orbital.

Quantitative estimates of MO x-ray–emission probabilities can now be obtained. First, assuming charge equilibration in the L and M shells, $P_{1s\sigma}$ can be calculated using the Meyerhof vacancy-sharing formalism.[41] Second, a reasonable choice of $E_{x\,min}$ can be made through visual inspection of Figs. 4 and 6–8. Choosing $E_{x\,min}=5$ keV, Fig. 9 can then be used to extract the value of $R(E_{x\,min})$, yielding $R(5\text{ keV})\simeq0.12$ a.u. $\simeq6300$ fm. Third, the tables of Scofield[42] can be used to obtain $\Gamma_x(5\text{ keV})=1.410\times10^{-15}\text{ s}^{-1}$.

Table IV gives the values of $P_{1s\sigma}$, $I(b,E_{x\,min})$, and $P_{MO}(b,E_{x\,min})$ calculated using Eqs. (22) and (23) for the representative example of $b=1000$ fm. These values of P_{MO} agree to within an order of magnitude with numbers obtained by integrating the probabilities shown in Figs. 6–8. More cannot be expected within this simple model. The observation that $P_{MO}(b,E_{x\,min})$ is nearly independent of beam velocity results because the $1/v$ dependence of $I(b,E_{x\,min})$ is nearly canceled by the velocity dependence of $P_{1s\sigma}$.

V. CONCLUSIONS

The analysis of MO x-ray–emission spectra for slow Cl^{16+} + Ar collisions has produced the first experimental determinations of $2p\pi$-$1s\sigma$ transition energies as a function of internuclear distance R. This achievement was

TABLE IV. K-vacancy-sharing probabilities ($P_{1s\sigma}$) and molecular-orbital x-ray–emission probabilities (I,P_{MO}) for each beam energy assuming the typical example of $b=1000$ fm, with the choice of $E_{x\,min}=5$ keV, and tabulated value (Ref. 42) $\Gamma_x=1.410\times10^{-15}\text{ s}^{-1}$.

	E (MeV)			
	20	10	5	2.5
$P_{1s\sigma}$	0.35	0.29	0.22	0.15
$I(b,E_{x\,min})$	3.6×10^{-4}	5.0×10^{-4}	7.1×10^{-4}	1.0×10^{-3}
$P_{MO}(b,E_{x\,min})$	1.3×10^{-4}	1.5×10^{-4}	1.6×10^{-4}	1.5×10^{-4}

made possible by using the acceleration-deceleration method to produce K-shell-vacancy–bearing chlorine projectiles at very low velocities. Oscillatory structures exhibited in these MO x-ray spectra are caused by quantum-mechanical interference effects similar to those in rainbow scattering and those recently observed in transitions between Rydberg states in Na.[43]

Collision broadening in MO x-ray emission was investigated by examining the energy region above the classical cutoff energy where the oscillatory pattern changes over into a nearly-exponential tail. The velocity dependence of spectral decay widths extracted from the experimental results was in qualitative agreement with the predictions of existing models. The spectral decay widths were observed to have little or no dependence on impact parameter.

Analytical approaches based on the stationary-phase and uniform asymptotic approximations were used to extract MO transition energies versus R over a wide range. The results of the two methods are in good agreement with theoretical predictions, and they are consistent over the range of R where both are applicable.

ACKNOWLEDGMENTS

This work was supported by the Deutsche Forschungsgemeinschaft and the Fundamental Interactions Branch, Division of Chemical Sciences, Office of Basic Energy Sciences, U.S. Department of Energy, under Contract No. DE-AC02-76CH00016. Four of us (R.S., R.H., H.S-B., and I.T.) want to acknowledge the kind hospitality during their stay at Brookhaven National Laboratory. Finally, we would like to acknowledge the late G. Hummer, who contributed much time and effort to the development and assembly of the experimental equipment at Brookhaven.

APPENDIX A

In this appendix the stationary-phase approximation (SPA) will be discussed. The style and notation used conform to the development used earlier.[23]

For the regular SPA, consider the integral

$$J(\omega)=\int_{-\infty}^{\infty} g(t)\exp[if(\omega,t)]dt \ , \tag{A1}$$

where $f(\omega,t)$ is a linear function of the parameter ω and the following conditions are satisfied: (a) $g(t)$ is an even function of t, (b) $f(\omega,t)$ is an odd function of t (which means that f'' is also odd while f' is even), and (c) $f''>0$ for $t>0$, and $f''<0$ for $t<0$, i.e., f' has a single minimum at $t=0$.

It is also assumed that for some range of the parameter ω the SPA equation

$$f'(\omega,t)=0 \tag{A2}$$

has real roots. Using the substitutions

$$\begin{aligned} &f(\omega,t)\leftrightarrow\int_0^t[\omega-\omega(s)]ds \ , \\ &g(t)\leftrightarrow\frac{1}{2\sqrt{2\pi}}D(R(t)) \ , \end{aligned} \tag{A3}$$

it is easy to check that conditions (a)–(c) are satisfied by the functions in Eq. (1). The range of ω for which Eq. (A2) has real roots is $\omega_\infty<\omega<\omega(0)$ when ω_∞ is the asymptotic value of $\omega(t)$ for $t\to\pm\infty$.

Using standard SPA,[31] $J_k(\omega)$, the contribution from the surroundings of any root t_k of Eq. (A2) to $J(\omega)$ is given by

$$J_k(\omega)=\left[\frac{2\pi}{|f''(t_k)|}\right]^{1/2} g(t_k) \times\exp\left[i\left[f(\omega,t_k)+\frac{\pi}{4}\mathrm{sgn}f''(t_k)\right]\right] . \tag{A4}$$

Assuming that ω is in the proper range, Eq. (A2) has exactly two real roots [a result of conditions (b) and (c) above], t_1 and t_2, where $t_1>0$ and $t_2=-t_1<0$. Also, it follows from the symmetry properties of f and g that the contributions from t_1 and t_2 are complex conjugates. Summing both contributions yields

$$J(\omega)\approx 2\left[\frac{2\pi}{f_1''}\right]^{1/2} g_1\cos\left[f_1+\frac{\pi}{4}\right] . \tag{A5}$$

It should be noted that the result blows up when $f_1''\to 0$. This problem can be traced to the fact that in this case the expansion $f(\omega,t)\approx f(\omega,t_1)+f''(t_1)(t-t_1)^2/2$, which is used in the framework of the SPA, is not justified. Assuming that $f'''(t_1)\neq 0$, $J(\omega)$ can still be evaluated using the next cubic term in the Taylor expansion of f. The solution contains Airy functions,[31] but the applicability of the approach is limited to a narrow range of ω values.

$D(\omega)$ is obtained from Eq. (A5) using the substitutions specified in Eq. (A3). The result is

$$D(\omega)=\frac{D_1}{(-\omega_1')^{1/2}}\cos\left[\int_0^{t_1}[\omega-\omega(s)]ds+\frac{\pi}{4}\right] . \tag{A6}$$

The ω dependence of $D(\omega)$ is mainly in the cosine term. The coefficient is nearly constant, so that Eq. (A6) can be replaced by the relation

$$D(\omega)\propto\cos\left[\int_0^{t_1} s\frac{d\omega(s)}{ds}ds+\frac{\pi}{4}\right] , \tag{A7}$$

where the integral was transformed using integration by parts and the fact that $\omega(t_1)=\omega$, which comes from the stationary-phase condition Eq. (A2). The use of the SPA in the evaluation of Eq. (A1) is justified when t_1 and t_2 are far enough apart, so that their contributions to the integral can be evaluated independently and when $g(t)$ is slowly changing around t_1 and t_2. Those statements can be formulated quantitatively as

$$\frac{f_1''}{t_1^2}\ll 1 \tag{A8}$$

and

$$\left|\frac{f'''}{(f'')^2}\frac{g'}{g}\right|\ll 1 . \tag{A9}$$

The derivation of these results, which is straightforward but tedious, will not be given here.

When ω is such that $f'(\omega,0)\to 0$, both t_1 and t_2 tend to zero. It can be shown that in this region Eqs. (A8) and (A9) cannot be satisfied. Keeping in mind that $f''(0)=0$ identically [see condition (b) above], the SPA cannot be used when the roots of Eq. (A2) are too close to zeros of f''. Inspection of Eq. (A6) immediately reveals that this forbidden ω region is that of $\omega\sim\omega(0)$, i.e., near the classical cutoff frequency.

APPENDIX B

In this appendix the uniform asymptotic approximation (UAA) will be discussed. This approximation extends the useful range of the SPA (discussed in Appendix A) and includes the SPA as a special case.

Following Connor and Marcus,[31] a new variable z is introduced,

$$f(\omega,t)=\tfrac{1}{3}z^3-\xi(\omega)z+A(\omega)\ , \tag{B1}$$

where A and ξ are constants which are chosen so as to make

$$\begin{aligned} t=t_1 &\leftrightarrow z=\xi^{1/2}\ , \\ t=t_2 &\leftrightarrow z=-\xi^{1/2}\ , \end{aligned} \tag{B2}$$

and where t_1 and t_2 are the roots of Eq. (A2), as before. It can be shown that A and ξ can be chosen to be positive for real roots and negative for complex t_1 and t_2.

By now it is assumed that the roots t_1 and t_2 are real (and therefore $t_2=-t_1$). Substituting Eq. (B2) into Eq. (B1) and solving for ξ and A yields

$$\begin{aligned} A&=0\ , \\ \xi&=(-\tfrac{3}{2}f_1)^{2/3}\ , \end{aligned} \tag{B3}$$

where the fact that f is odd and $f_1<0$ was used.

Substitution of Eq. (B1) into Eq. (A1), while using the results of Eq. (B3), yields

$$J_1(\omega)=\int_{-\infty}^{\infty} g(t(z))\frac{dt}{dx}\exp[i(\tfrac{1}{3}z^3-\xi z)]dz\ , \tag{B4}$$

where $g(dt/dz)$ can be expanded in powers of z. As any term starting from second order up can be transformed into a combination of zero- and first-order terms using integration by parts in Eq. (B4), the expansion can be written as

$$g\frac{dt}{dz}=p+qz\ . \tag{B5}$$

Substituting Eq. (B2) into Eq. (B5) and solving for p and q yields

$$\begin{aligned} p&=\tfrac{1}{2}g_1\left[\left.\frac{dt}{dz}\right|_1+\left.\frac{dt}{dz}\right|_2\right]\ , \\ q&=\frac{g_1}{2\xi^{1/2}}\left[\left.\frac{dt}{dz}\right|_1-\left.\frac{dt}{dz}\right|_2\right]\ . \end{aligned} \tag{B6}$$

Finally, differentiating Eq. (B1) twice, substituting Eq. (B2), and using the fact that $f_1'=f_2'=0$ yields

$$\left.\frac{dt}{dz}\right|_1=\left.\frac{dt}{dz}\right|_2=\left[\frac{2\xi^{1/2}}{f_1''}\right]^{1/2}\ , \tag{B7}$$

and therefore

$$\begin{aligned} p&=g_1\left[\frac{2\xi^{1/2}}{f_1''}\right]^{1/2}\ , \\ q&=0\ . \end{aligned} \tag{B8}$$

Substituting into Eq. (B4) finally results in

$$\begin{aligned} J(\omega)&=g_1\left[\frac{2\xi^{1/2}}{f_1''}\right]^{1/2}\int_{-\infty}^{\infty}\exp[i(\tfrac{1}{3}z^3-\xi z)]dz \\ &=2\pi g_1\left[\frac{2\xi^{1/2}}{f_1''}\right]^{1/2}\mathrm{Ai}(-\xi)\ . \end{aligned} \tag{B9}$$

It is interesting to check the behavior of Eq. (B9) for the limiting cases $\xi\gg 0$ and $\xi\ll 0$. Using Eq. (B3) and the asymptotic form of $\mathrm{Ai}(-\xi)$, the result for $\xi\gg 0$ is

$$\xi=J(\omega)\approx 2\left[\frac{2\pi}{f_1''}\right]^{1/2}g_1\cos\left[f_1+\frac{\pi}{4}\right]\ , \tag{B10}$$

which is identical with Eq. (A5). The case of $\xi\ll 0$, which corresponds to complex roots of Eq. (A2), cannot be derived directly from Eq. (B9), as Eq. (B9) itself was derived assuming that the roots are real. However, Connor's procedure can be repeated for this case and the result for $\xi\ll 0$, up to constant phase, is

$$\xi=J(\omega)\approx\left[\frac{2\pi}{|f_1''|}\right]^{1/2}g_1\exp(-|\mathrm{Im}f_1|)\ . \tag{B11}$$

Another interesting case is that of $\xi\to 0$, which corresponds to $f_1''\to 0$. Unlike the result of the SPA, the expression for $J(\omega)$ in Eq. (B9) converges in this case to a finite limit when $\xi\to 0$ of

$$\xi=J(\omega)\approx 2\pi g(0)\left[\frac{2}{f'''(0)}\right]^{1/3}\mathrm{Ai}(0)\ , \tag{B12}$$

which is identical to the result of the modified (cubic) SPA.

Now, $D(\omega)$ is obtained from $I(\omega)$ in Eq. (B9) using the substitution in Eq. (A3), which results in

$$\begin{aligned} D(\omega)=&\left[\frac{\pi\left[-\frac{3}{2}\int_0^{t_1}[\omega-\omega(s)]ds\right]^{1/3}}{-\omega_1'}\right]^{1/2} \\ &\times D_1\mathrm{Ai}\left[-\left[-\tfrac{3}{2}\int_0^{t_1}[\omega-\omega(s)]ds\right]^{2/3}\right]\ , \end{aligned} \tag{B13}$$

where the special cases discussed above, i.e., $\xi\gg 0$, $\xi\ll 0$, and $\xi\to 0$, correspond to $\omega\ll\omega(0)$, $\omega\gg\omega(0)$, and $\omega\to\omega(0)$, respectively.

In parallel with the discussion in Appendix A, the coefficient of the Airy function in Eq. (B13) is very weakly dependent on ω. Therefore, to good approximation, the coefficient can be taken as a constant, and Eq. (B13) can be replaced by the relation

$$D(\omega)\propto\mathrm{Ai}[-(\tfrac{3}{2}f_1)^{2/3}]\ . \tag{B14}$$

*Present address: Physics Division, Oak Ridge National Laboratory, P.O. Box X, Oak Ridge, TN 37831-6377.

†Present address: Siemens Aktiengesellschaft, München, Federal Republic of Germany.

[1]J. S. Briggs and K. Taulbjerg, in *Structures and Collisions of Ions and Atoms,* edited by I. A. Sellin (Springer-Verlag, Berlin, 1978), p. 105; P. H. Mokler and F. Folkmann, *ibid.*, p. 201.

[2]U. Wille and R. Hippler, Phys. Rep. **132**, 131 (1986).

[3]D. Schwalm, in *Physics of Electronic and Atomic Collisions,* edited by J. Eichler, I. Hertel, and N. Stolterfoht (North-Holland, Amsterdam, 1984), p. 295.

[4]R. Anholt, Rev. Mod. Phys. **57**, 995 (1985).

[5]D. Liesen, P. Armbruster, F. Bosch, S. Hagman, P. H. Mokler, H. Schmidt-Böcking, R. Schuch, J. B. Wilhelmy, and H. J. Wollersheim, Phys. Rev. Lett. **44**, 983 (1980).

[6]M. A. Herath-Banda, A. V. Ramaya, C. F. Maguire, F. Güttner, W. Koenig, B. Martin, B. Povh, H. Skapa, and J. Soltani, Phys. Rev. A **29**, 2429 (1984).

[7]See, e.g., the following recent reviews: W. Meyerhof, Science **3**, 839 (1976); W. Lichten, J. Phys. Chem. **84**, 2102 (1980).

[8]P. H. Mokler, H.-J. Stein, and P. Armbruster, Phys. Rev. Lett. **29**, 827 (1972).

[9]F. W. Saris, W. F. van der Weg, H. Tawara, and R. Laubert, Phys. Rev. Lett. **28**, 717 (1972).

[10]J. R. Macdonald, M. D. Brown, and T. Chiao, Phys. Rev. Lett. **30**, 471 (1973).

[11]G. Bissinger and L. C. Feldman, Phys. Rev. Lett. **33**, 1 (1975).

[12]J. H. Macek and J. S. Briggs, J. Phys. B **7**, 1312 (1974).

[13]J. S. Greenberg, C. K. Davis, and P. Vincent, Phys. Rev. Lett. **33**, 473 (1974).

[14]V. Weiskopf, Phys. Z. **34**, 1 (1933).

[15]B. Müller, R. Kent-Smith, and W. Greiner, Phys. Lett. B **49**, 219 (1974).

[16]I. Tserruya, H. Schmidt-Böcking, R. Schulé, R. Schuch, and H. J. Specht, Phys. Rev. Lett. **36**, 1451 (1976).

[17]J. S. Briggs and K. Dettman, J. Phys. B **10**, 1113 (1977).

[18]W. Wölfli, E. Morenzoni, Ch. Stoller, G. Bonani, and M. Stockli, Phys. Lett. A **68**, 217 (1978).

[19]See, e.g., R. Anholt, Z. Phys. A **288**, 257 (1978).

[20]I. Tserruya, R. Schuch, H. Schmidt-Böcking, J. Barrette, Wang Da-Hai, B. M. Johnson, K. W. Jones, and M. Meron, Phys. Rev. Lett. **50**, 30 (1983).

[21]R. Schuch, H. Schmidt-Böcking, I. Tserruya, B. M. Johnson, K. W. Jones, M. Meron, Z. Phys. A **320**, 185 (1985).

[22]See P. Theiberger, J. Barrette, B. M. Johnson, K. W. Jones, M. Meron, and and H. E. Wegner, IEEE Trans. Nucl. Sci. **NS-30**, 1431 (1983), and references therein.

[23]M. Meron, B. M. Johnson, K. W. Jones, R. Schuch, H. Schmidt-Böcking, and I. Tserruya, Nucl. Instrum. Methods B **10/11**, 64 (1985).

[24]G. Gaukler, H. Schmidt-Böcking, R. Schuch, R. Schulé, H. J. Specht, and I. Tserruya, Nucl. Instrum. Methods **141**, 115 (1977).

[25]M. Meron, D. Maor, and B. Rosner, J. Phys. B **16**, 3983 (1983).

[26]P. Kienle, M. Kleber, B. Povh, R. M. Diamond, F. S. Stephens, E. Grosse, M. R. Maier, and D. Proetel, Phys. Rev. Lett. **31**, 1099 (1973).

[27]R. Schuch, G. Gaukler, H. Schmidt-Böcking, Z. Phys. A **290**, 19 (1979).

[28]R. Hoffman, Ph.D. thesis, University of Heidelberg, 1983 (unpublished); R. Hoffmann, E. Justiniano, and R. Schuch (unpublished).

[29]W. Fritsch and U. Wille, Jpn. J. Appl. Phys. **17**, Suppl. 17-2, 387 (1978); J. Phys. B **12**, L335 (1979).

[30]C. Chester, B. Friedman, and F. Ursell, Proc. Cambridge Philos. Soc. **53**, 599 (1957).

[31]J. N. L. Connor and R. A. Marcus, J. Chem. Phys. **55**, 5636 (1971).

[32]A. Z. Devdariani, U. N. Ostroskii, and A. Niehaus, J. Phys. B **18**, L161 (1985).

[33]A. Niehaus, in *Electronic and Atomic Collisions,* edited by D. C. Lorents, W. E. Meyerhof, and J. R. Peterson (Elsevier, Amsterdam, 1986), p. 657.

[34]D. R. Bates and R. H. Reid, Adv. Atom. Mol. Phys. **4**, 13 (1968).

[35]K. H. Heinig, H. U. Jäger, H. Richter, H. Woittenek, W. Frank, P. Gippner, K. H. Kaun, and P. Manfrass, J. Phys. B **10**, 1321 (1977).

[36]B. Fricke, W.-D. Sepp, and T. Morovic, Z. Phys. A **318**, 369 (1984).

[37]B. Müller, in *Electronic and Atomic Collisions,* edited by J. S. Risley and R. Geballe (University of Washington Press, Seattle, 1976), p. 481.

[38]H. D. Betz, F. Bell, H. Panke, W. Stehling, E. Spindler, and M. Kleber, Phys. Rev. Lett. **34**, 1256 (1975).

[39]H. Schmidt-Böcking, R. Schuch, I. Tserruya, R. Schulé, H. J. Specht, and K. Bethge, Z. Phys. A **284**, 39 (1978).

[40]P. Vincent and J. S. Greenberg, J. Phys. B **12**, L641 (1979).

[41]W. E. Meyerhof, Phys. Rev. Lett. **31**, 1341 (1973).

[42]J. H. Scofield, Phys. Rev. **179**, 9 (1969).

[43]J. Singh, X. Sun, and K. B. McAdam, Phys. Rev. Lett. **58**, 2201 (1987).

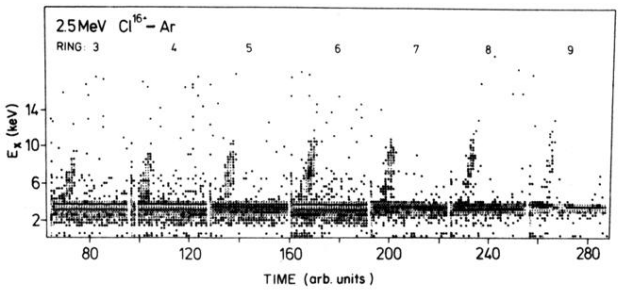

FIG. 5. Two-dimensional event plots of coincidence time vs x-ray energy for different rings of the PPAD particle detector.